The Influence of Atmospheric Cloud Radiative Effects on the Large-Scale Stratospheric Circulation

Ying Li* and David W. J. Thompson

Department of Atmospheric Science, Colorado State University, Fort Collins, Colorado, USA

Yi Huang

Department of Atmospheric and Oceanic Sciences, McGill University, Montreal, Quebec, Canada

Corresponding author address: Ying Li, Department of Atmospheric Science, Colorado State University, 3915 W. Laporte Ave. Fort Collins, CO 80521

E-mail: yingli@atmos.colostate.edu

ABSTRACT

Previous studies have explored the influence of atmospheric cloud radiative effects (ACRE) on the tropospheric circulation. Here the authors explore the influence of ACRE on the *stratospheric* circulation. The response of the stratospheric circulation to ACRE is assessed by comparing simulations run with and without ACRE. The stratospheric circulation response to ACRE is reproducible in a range of different GCMs, and can be interpreted in the context of both a dynamically-driven and a radiatively-driven component.

The dynamic component is linked to ACRE-induced changes in the vertical and meridional fluxes of wave activity. The ACRE-induced changes in the vertical flux of wave activity into the stratosphere are consistent with the ACRE-induced changes in tropospheric baroclinicity and thus the amplitude of midlatitude baroclinic eddies. They account for a strengthening of the Brewer-Dobson circulation, a cooling of the tropical lower stratosphere, a weakening and warming of the polar vortex, a reduction of static stability near the tropical tropopause transition layer, and a shortening of the timescale of extratropical stratospheric variability. The ACRE-induced changes in the equatorward flux of wave activity in the low latitude stratosphere account for a strengthening of the zonal wind in the subtropical lower-middle stratosphere.

The radiative component is linked to ACRE-induced changes in the flux of longwave radiation into the lower stratosphere. The changes in radiative fluxes lead to a cooling of the extratropical lower stratosphere, changes in the static stability and cloud fraction near the extratropical tropopause, and a shortening of the timescales of extratropical stratospheric variability.

The results highlight a previously overlooked pathway through which tropospheric climate influences the stratosphere.

1. Introduction

Atmospheric cloud radiative effects (ACRE) are defined as the difference between cloud radiative effects at the top of the atmosphere and the surface. They are dominated by the longwave component, as shortwave cloud radiative effects are mainly manifested at the surface (Allan 2011; Haynes et al. 2013). ACRE have an important influence on both the vertical and horizontal distribution of atmospheric diabatic heating. Hence they can have a profound impact on the atmospheric circulation in both the tropical and extratropical atmosphere.

Numerous studies have explored the influence of ACRE on the tropospheric circulation. ACRE have been shown to influence the mean tropical circulation (Slingo and Slingo 1988, 1991; Randall et al. 1989; Gordon 1992; Sherwood et al. 1994; Tian and Ramanathan 2003; Fermepin and Bony 2014; Li et al. 2015); the location of the intertropical convergence zone (ITCZ; Voigt et al. 2014; Harrop and Hartmann 2016), the development and maintenance of convective self-aggregation (Bretherton et al. 2005; Muller and Held 2012; Wing and Emanuel 2014; Coppin and Bony 2015; Muller and Held 2015); and the structure of the large-scale extratropical circulation (Li et al. 2015).

ACRE have also been shown to influence tropical tropospheric variability on intraseasonal and interannual timescales. For examples, Crueger and Stevens (2015) demonstrated that ACRE amplifies the amplitude of the Madden-Julian Oscillation (MJO) in numerical simulations by modulating the vertical profile of heating and Rädel et al. (2016) revealed that the simulated coupling between cloud radiative effects and the large-scale tropospheric circulation can amplify variability in the El Niño/Southern Oscillation.

Recent experiments have also highlighted the influence of ACRE on the tropospheric circulation response to climate change (Voigt and Shaw 2015, 2016; Merlis 2015; Ceppi and Hartmann 2016).

Voigt and Shaw (2015) suggested that differences in ACRE contribute to differences in the tropical precipitation and circulation response to climate change. Merlis (2015) proposed that cloud masking of radiative forcing contributes to the weakening of the tropical circulation in response to increasing CO2. Ceppi and Hartmann (2016) argued that cloud radiative effects (mainly those associated with shortwave radiation) play a key role in the atmospheric circulation response to CO2 forcing by enhancing the meridional temperature gradient at all levels in the troposphere.

In this contribution, we highlight the influence of ACRE on the stratospheric circulation, which to our knowledge has not been emphasized in previous work. The current study may be viewed as a companion study to Li et al. (2015). In that study, we demonstrated that ACRE have a robust influence on the simulated global tropospheric circulation. Here we demonstrate that ACRE also have a robust influence on the global stratospheric circulation.

2. Numerical experiments

There are two commonly applied methodologies for assessing the influence of cloud radiative effects on the atmospheric circulation in numerical simulations. One is to fix cloud radiative properties to their control values at every call in the radiation code (the "cloud-locking" method). The locking method has been used to quantify various radiative feedbacks (e.g., Wetherald and Manabe 1980, 1988; Hall and Manabe 1999; Schneider et al. 1999; Mauritsen et al. 2013), to isolate the atmospheric circulation response to cloud radiative effects from the direct radiative forcing of $4\times$CO2 (Ceppi and Hartmann 2016; Voigt and Shaw 2016), and to explore the climate response to the suppression of cloud/circulation interactions (Rädel et al. 2016). A second method is to turn off cloud radiative effects at every call in the radiation code (e.g., Slingo and Slingo 1988; Randall et al. 1989; Slingo and Slingo 1991; Stevens et al. 2012; Fermepin and Bony 2014; Crueger and Stevens 2015; Li et al. 2015; Merlis 2015; Harrop and Hartmann 2016). The second

approach induces large changes in the top of the atmosphere radiative fluxes, hence it is typically applied in simulations run with prescribed sea-surface temperatures (SSTs) to avoid climate drift. Fixing SSTs minimizes the effects of changes in surface shortwave cloud radiative effects, and thus the second approach limits analyses to the role of longwave atmospheric cloud radiative effects on the circulation.

Here we exploit the second approach to explore the influence of ACRE on the long-term mean stratospheric flow. To do so, we use output of Atmospheric Model Intercomparison Project (AMIP) style experiments conducted under the auspices of the COOKIE (the Clouds On-Off Klima Intercomparison Experiment) simulation. Details of the experiments are provided in Appendix A and Stevens et al. (2012). In brief, the COOKIE project provides a framework for exploring the circulation response to ACRE in a variety of numerical models and experiment set-ups (Stevens et al. 2012). We focus on two AMIP-type experiments from the atmospheric component of the Institut Pierre Simon Laplace (IPSL) coupled climate model (version IPSL-CM5A-LR; Dufresne et al. 2013): 1) a 30-yr control "clouds-on" experiment in which the full suite of ACRE are included in the simulations and 2) a 30-yr "clouds-off" experiment in which model ACRE are turned off in the radiative code. The two experiments are forced by the same observed monthly-mean SSTs and sea-ice concentrations over the period 1979–2008. Thus, the differences between clouds-on and clouds-off experiments uniquely reveal the impact of ACRE on the model climate given identical surface boundary conditions. The robustness of the primary results in other numerical models available through the COOKIE project is reviewed in the Discussion.

Figure 1 briefly reviews the long-term mean atmospheric circulation derived from the "clouds on" simulation (left panels) and compares it with that derived from European Centre for Medium-Range Weather Forecasts interim reanalysis (ERA-Interim; Simmons et al. 2007). Details of the calculation of the fields shown in Fig. 1 are given in Appendix B. The climatological-mean

circulation of the atmospheric component of the IPSL coupled climate model was also reviewed in Li et al. (2015), but the discussion there focused on circulation features at tropospheric levels. Here we focus on the circulation at stratospheric levels.

The key point in Figure 1 is that the atmospheric component of the IPSL model closely captures key aspects of the climatological-mean stratospheric circulation. These include (e.g., Andrews et al. 1987):

- westerly jets at mid-high latitudes that extend poleward and upward from the midlatitude tropopause in both hemispheres (Figs. 1a,b). The relatively weak amplitude of the Northern Hemisphere (NH) polar vortex reflects hemispheric differences in generating the upward propagating, hemispheric-scale Rossby waves.

- equator-to-pole residual mass overturning cells in both hemispheres, with upwelling at the tropical tropopause and downwelling in the mid-high latitude stratosphere (Figs. 1c,d). Both the model and observed Brewer-Dobson circulations are centered slightly north of the Equator in the annual-mean.

- vertically propagating wave activity at stratospheric levels that bends equatorward in the middle stratosphere and dissipates at both subtropical and extratropical latitudes (Figs. 1e,f). The wave dissipation is the principal forcing of the stratospheric residual circulation indicated in panels c and d (e.g., Andrews et al. 1987; Haynes et al. 1991).

3. The influence of ACRE on the stratospheric circulation

Figure 2 shows the simulated ACRE in the IPSL model. The figure is reproduced from Li et al. (2015) and shows only the longwave component of the ACRE, since it dominates the cloud radiative forcing within the atmosphere. As discussed in Li et al. (2015), the primary features in

the zonal-mean ACRE include 1) radiative cooling in the upper troposphere near the tropopause level due to the emission of longwave radiation from cloud tops, and 2) radiative warming in the middle troposphere due to the trapping of outgoing longwave radiation by middle- and upper-level clouds.

Figures 3-5 show the differences in various key fields when the ACRE indicated in Fig. 2 are included in the radiation code. Since all parameters other than ACRE are held fixed between the two runs, the "clouds-on" − "clouds-off" results shown in Figs. 3-5 reflect the influence of ACRE on the model circulation. Figure 3 shows the differences in zonal-mean temperature, zonal-mean zonal wind, and the residual mass streamfunction. Figure 4 shows the differences in the Eliassen-Palm flux (EP flux; top), and the wavenumber decomposition of the difference in the EP fluxes at key levels (bottom and middle). Figure 5 shows the differences in static stability and cloud fraction. Stippling indicates regions where the differences are significant at the 99% confidence level by using a two-tailed test of the *t* statistics assuming 30 degree of freedom with 30-year long annual-mean data.

The tropospheric response to ACRE is discussed in Li et al. (2015) and consists primarily of 1) increases in the meridional temperature gradient and thus baroclinicity in the sub-tropical upper troposphere (Fig. 3a); 2) anomalous westerly flow centered $\sim 40^\circ$ and easterly flow centered $\sim 65^\circ$ (Fig. 3b); 3) anomalously upward wave fluxes (poleward eddy heat fluxes) in the upper troposphere at midlatitudes (Fig. 4a); and 4) anomalously equatorward wave fluxes (poleward eddy momentum fluxes) in the upper troposphere equatorward of $\sim 45^\circ$ (Fig. 4a).

The stratospheric component of the response to ACRE is clearly substantial but has not been explored in previous work. The primary differences in the stratospheric flow include:

- cooling in the lower stratosphere at tropical latitudes centered around ∼70 hPa, juxtaposed against relatively weak warming at mid/high latitudes above 70 hPa (Fig. 3a).

- decreases in static stability in the upper troposphere juxtaposed against increases in static stability in the lower stratosphere (Fig. 5a). The changes in the static stability derive primarily from the cooling of the lowermost stratosphere (Fig. 3a) and reflect a strengthening and upward shift of the tropopause inversion layer (TIL; Birner et al. 2002; Birner 2006).

- widespread increases in cloud fraction near the tropopause (Fig. 5b). As noted in Li et al. (2015), the changes in cloud fraction are consistent with the local decreases in static stability (Fig. 5a) and rising of the tropopause (see Fig. 3a). As discussed later, they likely play an important role in radiative coupling between the model stratospheric and tropospheric circulations.

- westerly changes in the zonal flow below 30 hPa centered around 30–40° juxtaposed against easterly changes around 70° (Fig. 3b). The changes in the stratospheric flow indicate a weakening and slight equatorward shift of the stratospheric polar vortices.

- increases in upwelling in the tropical stratosphere juxtaposed against enhanced downwelling at extratropical latitudes (Fig. 3c). The changes in the stratospheric mass streamfunction reflect a $\sim 20\%$ strengthening of the model BDC.

- increases in the vertical flux of wave activity (and thus the poleward eddy heat flux) in the lower extratropical stratosphere (Figs. 4a).

- changes in meridional wave propagation (and thus the meridional eddy momentum flux) in the lower stratosphere. Waves are generally bent anomalously equatorward at low latitudes equatorward of ∼45° (Figs. 4a).

What physical processes drive the changes in the model stratospheric circulation that result from the inclusion of ACRE? The changes in the stratospheric circulation shown in Figs. 3-5 can be viewed in the context of two components: 1) a *dynamical* component that is consistent with the changes in the fluxes of wave activity both into the lower stratosphere and within the stratosphere, and 2) a *radiative* component that is consistent with the changes in the flux of longwave radiation into the lower stratosphere.

Much of the response in the stratospheric zonal flow and meridional overturning circulation to ACRE are consistent with the *dynamical* component. The amplitude of the stratospheric meridional overturning circulation is linked to the propagation of both synoptic and planetary scale waves into the extratropical stratosphere, and different wave types play different roles in driving the circulation at different levels (e.g., Yulaeva et al. 1994; Randel et al. 2008; Ueyama and Wallace 2010; Birner and Boñisch 2011; Ueyama et al. 2013; Grise and Thompson 2013). The strengthening of the model BDC, the cooling of the tropical stratosphere, the relatively weak warming of the mid/high latitude stratosphere above 70 hPa, and the easterly changes in the high latitude flow extending to the upper troposphere are all consistent with the enhanced upward propagation of wave activity from the troposphere to the stratosphere (Figs. 4a). The westerly anomalies in the midlatitude stratosphere below 30 hPa (Fig. 3b) are consistent with the anomalous poleward momentum fluxes centered near 30-40°, which arise from the anomalous equatorward refraction of stratospheric wave fluxes at low latitudes (Figs. 4a).

Figure 4b examines the wavenumber decomposition of the changes in the vertical flux of wave activity between 500–200 hPa (where the meridional and vertical structures of the ACRE are distinct; see Fig. 2), and Figure 4c examines the wavenumber decomposition of the changes in the meridional flux of wave activity in the upper troposphere between 200–300 hPa (where amplitudes of the eddy fluxes of momentum are largest; see. Fig. 6a in Li et al. 2015). Note that we

focus on the vertical fluxes in the upper troposphere since the source of the stratospheric wave drag ultimately derives from the uppermost troposphere. The increases in the vertical flux of wave activity derive from two primary features: 1) enhanced heat fluxes associated with wavenumbers ∼4–6 between 30–50°, and 2) enhanced heat fluxes associated with wavenumbers ∼2–3 between 50-70°, particularly in the NH. The increases associated with wavenumbers ∼4–6 are consistent with the increases in baroclinic wave amplitudes in regions of enhanced baroclinicity (see Fig. 9 in Li et al. 2015). The increases in upper tropospheric baroclinicity are, in turn, driven directly by the meridional structure of the ACRE, e.g., between 500-200 hPa, ACRE heat the free troposphere at low latitudes but cool it at high latitudes (Fig. 2). The largest increases in the equatorward propagation of wave activity in the upper troposphere derive primarily from eddies with wavenumbers ∼3–6, i.e., synoptic scale waves. Interestingly, Eichelberger and Hartmann (2005) find very similar changes in wave activity and the strength of the BDC in simulations run with imposed tropical tropospheric warming.

The cooling of the extratropical lower stratosphere and the associated changes in near tropopause static stability are consistent with the *radiative* component of the stratospheric response. (The cooling of the extratropical lowermost stratosphere is the opposite sign of that expected from the changes in the BDC, and thus can not be driven by the changes in stratospheric wave drag). That is: The pattern of ACRE includes large cooling in the extratropical upper troposphere (Fig. 2) where the upward emission of longwave radiation by cloud tops exceeds the incident radiation from above. The inclusion of ACRE in the "clouds-on" simulation thus acts to decrease static stability near the extratropical tropopause which, in turn, leads to increases in cloud fraction there (Fig. 5b, see also the discussion in Li et al. 2015). The increases in cloud fraction lead to an increase in the radiative cooling of the extratropical tropopause and thus to cooling of the extratropical lower stratosphere (Fig. 3a). As discussed further in Section 4, the increases in cloud fraction near the

extratropical tropopause also contribute to a shortening of the radiative timescales in the lowermost stratosphere due to the increased emissivity of the near-tropopause region (see Eq. B18).

The dynamical and radiative forcing of the stratospheric circulation induced by ACRE is not uniform throughout the year. Figure 6 highlights the seasonal cycle of the dynamical and radiative components of the forcing at upper tropospheric levels (200–300 hPa), where ACRE exhibit a robust meridional gradient (Fig. 2). Figure 6a shows the seasonal cycle of the differences in cloud longwave heating rates (i.e., cloud radiative heating rate in clouds-on experiment, recall that the cloud-induced radiative heating rate is zero in clouds-off experiments); Figure 6b the dynamical component of the forcing indicated by the differences in the wavenumbers 4–6 component of the vertical flux of wave activity (which contributes primarily to the changes in vertical flux of wave activity into the lower stratosphere; Fig. 4b); and Figure 6c the radiative component of the forcing indicated by the differences in cloud fraction (which correspond closely to the cloud longwave radiative cooling at extratropics). The changes in all three fields peak during the cold season months in both hemispheres. At this time, the meridional gradients in cloud radiative heating between the tropics and extratropics are largest (panel a), and so are the changes in 1) upper tropospheric baroclinicity (not shown); 2) the generation of baroclinic wave activity (as inferred by the increases in heat fluxes associated with wavenumbers 4–6; panel b); and 3) cloud fraction (panel c).

4. Projection onto the timescales of stratospheric variability

In this section, we examine the changes in the timescales of stratospheric dynamic variability which, in turn, are linked to the radiative timescales in the lowermost stratosphere.

Figure 7 shows the *e*-folding timescale of the autocorrelation function of the NH extratropical zonal-mean zonal wind and temperature anomalies as a function of latitude and height for the

winter season months January–March (JFM). The details of the calculation of the *e*-folding time scale are provided in Appendix B. In the clouds-on experiment, the simulated *e*-folding time scales are greatest in the extratropical zonal wind field around 55°N and 70 hPa and in the extratropical temperature field poleward of 60°N between ∼100–200 hPa. In these regions, the memory in the flow is roughly comparable to observational estimates of the timescales of the northern annular mode, or ∼40 days (Baldwin et al. 2003; Gerber et al. 2008). Interestingly, the *e*-folding autocorrelation time scale is considerably longer in the clouds-off experiments than it is in the clouds-on experiments (∼65 vs. ∼40 days). The persistence of the extratropical stratospheric circulation is unrealistically long in the absence of ACRE.

Understanding the timescale of the lowermost extratropical winter stratosphere has important implication for two-way coupling between the stratosphere and troposphere (Baldwin et al. 2003). The slowly varying circulations in the wintertime lower stratosphere have been shown to propagate downward into the troposphere (e.g., Kodera et al. 1990; Baldwin and Dunkerton 1999), where they contribute to the predictability of the tropospheric flow (e.g., Baldwin and Dunkerton 2001). The unrealistically long stratospheric timescales in the absence of ACRE may project onto an unrealistically persistent tropospheric response to stratosphere-troposphere coupling.

Figure 8 illustrates the effects of the contrasting stratospheric timescales in the clouds-on and clouds-off simulations on stratosphere/troposphere coupling. The figure shows zonal-mean zonal wind anomalies averaged between 55°–75°N regressed onto standardized JFM values of zonal-mean zonal wind anomalies at 10 hPa as a function of pressure level and lag. The lag regressions are based on daily anomaly data centered about the JFM season. By construction, positive anomalies in the zonal-mean zonal wind are largest at 10 hPa, day 0, and start decaying after day 0. It is evident that zonal-mean zonal wind anomalies are more persistent in the lower stratosphere in the clouds-off experiment than they are in the clouds-on experiment, and that the increased per-

sistence of the stratospheric flow projects onto the timescales of the circulation in the middle and lower troposphere (also see tropospheric levels Figs. 7a, b).

The decreased timescales of the extratropical stratospheric circulation in the clouds-on experiment can be explained by both the *dynamical* and *radiative* effects of ACRE on the stratospheric circulation. The *dynamical* effect follows from the increases in the vertical flux of wave activity into the extratropical stratosphere in the clouds-on simulation (Figs. 4a). Increases in the flux of wave activity will lead to a more disturbed stratospheric polar vortex and thus a shorter timescale of variability in the circulation.

The *radiative* effect follows from the enhanced radiative cooling of the upper extratropical troposphere in the cloud-on simulation (Fig. 2), and the inverse relationship between the magnitude of the local radiative cooling rate and the local radiative damping time scales (see Appendix B for the derivation). The negative ACRE imposed in the upper extratropical troposphere (Fig. 2) act to enhance the amplitude of the (already negative) clear-sky radiative cooling rates in the upper troposphere. The increased amplitude of the (negative) radiative cooling rates leads to shorter radiative damping time scales in the extratropical upper troposphere and lower stratosphere which, in turn, lead to lessened persistence of the stratospheric flow.

A quantitative estimate of the relative roles of dynamical and radiative processes in determining the timescale of stratospheric variability would require additional experiments with, for example, a radiative transfer model in which the dynamical forcing is held fixed and only the ACRE is changed between simulations. Such a quantitative investigation is beyond the scope of this study.

5. Summary and Discussion

The primary impacts of atmospheric cloud radiative effects on the stratospheric circulation are summarized in Fig. 9. We have argued that the responses can be viewed in the context of a *dynamic* component and a *radiative* component.

The *dynamic* component is consistent with the enhanced flux of wave activity into the lower stratosphere (Figs. 4a,b) and changes in the meridional propagation of wave activity within the stratosphere (Figs. 4a,c) when ACRE are included in the simulation. The increases in the vertical flux of wave activity are consistent with enhanced upper tropospheric baroclinicity and baroclinic wave amplitudes (see Li et al. 2015). They account for the strengthening of the BDC, the cooling of the tropical stratosphere juxtaposed against the relatively weak warming of the mid/high latitude stratosphere above $\sim$70 hPa (Fig. 3a), and the weakening of the zonal wind in the upper stratosphere at high latitudes. The enhanced equatorward flux of wave activity in the lower subtropical stratosphere accounts for strengthening of the westerly zonal flow in the subtropical lower and middle stratosphere (Figs. 3b).

The *radiative* component is consistent with enhanced cloud-top longwave cooling extending across the tropopause into the lower stratosphere due to increases in cloud fraction near the tropopause (Fig. 5b). It accounts for the cooling of the extratropical lower stratosphere, the decreases in static stability in the upper troposphere, and the increases in static stability in the lower stratosphere (Figs. 3a, 5a). Previous studies have suggested that the vertical structure of static stability at the tropopause level is strongly influenced by the radiative effects of water vapor (Randel et al. 2007). The results shown here suggest that the radiative effects of clouds also contribute notably to the structure of static stability in this region. The shorter timescale of the extratropical

stratospheric circulation in the clouds-on experiment are consistent with both the *dynamic* and *radiative* components of the responses.

The results shown here are based on output from one GCM (IPSL-CM5A-LR). To assess the robustness of the results, we reproduced key responses in six different GCMs also available through the COOKIE experiment. The GCMs examined are listed in Table 1; the key responses are highlighted in Table 2. The strengthening of the BDC, the warming in the upper polar stratosphere, the cooling in the tropical lower stratosphere, the weakening of the polar vortex, the weakening of static stability near the tropical tropopause transition layer, the cooling of the extratropical stratosphere, and the increases in the amplitude of the TIL are all generally robust across the range of GCMs indicated in Table 1. The inter-model spread in the amplitude of the responses could be due to 1) the differences in ACRE between one simulation and the next, 2) the differences in the model responses to the same ACRE, and/or 3) sampling variability. The vertically integrated ACREs are similar across all models (Fig. 10), which suggests differences in ACRE are not pronounced from one simulation to the next. However, to fully understand the inter-model spread in the amplitude of circulation responses in Table 2 would require analyses of the differences in the vertically-resolved ACREs which, unfortunately, are not provided in the COOKIE archive.

Previous work has established the impact of tropospheric dynamics on the stratospheric flow (e.g., Charney and Drazin 1961; Matsuno 1970), the impact of stratospheric dynamics on the tropospheric flow (e.g., Baldwin and Dunkerton 2001; Limpasuvan et al. 2004, 2005), the influence of stratospheric radiative fluxes on tropospheric temperatures (Forster et al. 2007; Grise et al. 2009), and the influence of stratospheric dynamics on tropospheric clouds (Li and Thompson 2013; Davis et al. 2013; Kohma and Sato 2014; Kodera et al. 2015). The results shown here provide a novel pathway through which stratospheric and tropospheric processes are coupled: via the influence of tropospheric cloud radiative effects on stratospheric climate. The results suggest

that model representations of ACRE are central in determining the mean stratospheric circulation, the distribution of stratospheric ozone and other constituents, and the timescale of extratropical stratospheric variability.

Acknowledgment. We thank Sandrine Bony (LMD) for providing the daily output "clouds-off" simulation on original vertical resolutions (39 levels). We also thank three anonymous reviewers, Sandrine Bony and Graeme Stephens for their helpful comments. YL is funded by NSF Climate and Large-Scale Dynamics (AGS-1547003) and NASA JPL (1439268). DWJT is funded by NSF Climate and Large-Scale Dynamics (AGS-1343080 and AGS-1547003). YH is funded by Discovery Program of the Natural Sciences and Engineering Council of Canada (RGPIN 418305-13) and the Team Research Project Program of the Fonds de recherché Nature et technologies of Quebec (PR-190145).

APPENDIX A

CFMIP COOKIE simulations

The Clouds On-Off Klimate Intercomparison Experiment (COOKIE Stevens et al. 2012) is performed under the auspices of the Cloud Feedback Model Intercomparison Project (CFMIP). In the clouds-off experiment, clouds are made transparent in the call to the radiation code. The clouds-on and clouds-off simulations are both run in an atmospheric model forced by the same prescribed sea surface temperatures. The differences in the circulation between the clouds-on and clouds-off simulations result entirely from differences in atmospheric cloud radiative effects (ACRE), which are dominated by the longwave component. To some degree they also derive from changes in land surface temperature, as the land surface temperature is not fixed and can thus feel the absence of cloud-radiative heating. To better isolate the role of ACRE on the circulation, COOKIE-like

experiments will be included in CMIP6 in which clouds are made transparent to radiation only in the longwave (Webb et al. 2016).

The primary results presented in this study are based on the COOKIE simulations generated by IPSL-CM5A-LR model. The atmospheric resolution of the IPSL-CM5A-LR is 3.75° latitude $\times$ 1.875° longitude mesh, and at 39 vertical levels on a hybrid sigma pressure coordinate system with the top level extending up to 0.04 hPa. The model output used in this study are essentially the same as those used in Li et al. (2015), but unlike in Li et al. (2015), the diagnostic terms (as described in Appendix B) are calculated based on 39 original sigma levels (as opposed to the interpolated 8 pressure levels used in Li et al. 2015) so as to better represent the fine-scale vertical structure of the stratospheric response.

We also performed selected analyses for six other different models available for the COOKIE set up. The details of the models are given in Table 1.

APPENDIX B

Diagnostic details

a. Calculations of the Eliassen-Palm Flux (EP) flux

In the quasi-geostrophic (QG) approximation, the Eliassen-Palm flux (EP flux) vector, denoted as **F**, in spherical and pressure coordinates (Edmon et al. 1980; Vallis 2006) can be written as:

$$F_\phi = -a\cos\phi[v^*u^*], \tag{B1}$$

$$F_p = fa\cos\phi\frac{[v^*\theta^*]}{[\theta]_p}, \tag{B2}$$

Here the bracket (asterisk) denotes zonal means (deviation from the zonal mean). a is the radius of Earth, ϕ is latitude, $f = 2\Omega\sin\phi$ is the Coriolis parameter, u and v are the zonal and meridional

velocity components. θ denotes potential temperature, and its partial derivative with respect to p is written as θ_p. The eddy fluxes are calculated based on daily-mean output and then averaged over the time period of interest.

The EP flux divergence term related to the acceleration of the zonal-mean zonal flow in the zonal-mean momentum equation is:

$$D_F \equiv \frac{1}{a\cos\phi}\nabla\cdot\mathbf{F}, \tag{B3}$$

with the flux divergence given by:

$$\nabla\cdot\mathbf{F} = \frac{1}{a\cos\phi}\frac{\partial}{\partial\phi}\left(F_\phi\cos\phi\right) + \frac{\partial}{\partial p}\left(F_p\right). \tag{B4}$$

For a graphical display of EP flux in latitude-pressure coordinates, the EP flux vectors are scaled according to Edmon et al. (1980, see Eq. 3.12). In addition, to enhance the visibility of the small vectors in the stratosphere, the EP flux is scaled by the square root of 1000/pressure (Taguchi and Hartmann 2006), and is scaled by a magnification factor of 5 above 100 mb.

The daily u, v, and θ fields are expanded into their Fourier harmonics, and the EP flux for zonal wave 1 to 10 are calculated.

Variations in the planetary wave EP flux entering the lower stratosphere are associated with changes in residual zonal-mean circulation ($[\tilde{v}]$, $[\tilde{w}]$; e.g., Haynes et al. 1991), defined by

$$[\tilde{v}] \equiv [v] - \frac{\partial}{\partial p}\left(\frac{[v^*\theta^*]}{[\theta]_p}\right), \tag{B5}$$

$$[\tilde{\omega}] \equiv [\omega] + \frac{1}{a\cos\phi}\frac{\partial}{\partial\phi}\left(\frac{[v^*\theta^*]}{[\theta]_p}\cos\phi\right). \tag{B6}$$

The quantities $[\tilde{v}]$ and $[\tilde{w}]$ are linked by a continuity equation

$$\frac{1}{a\cos\phi}\frac{\partial}{\partial\phi}([\tilde{v}]\cos\phi) + \frac{1}{\rho_0}\frac{\partial}{\partial z}(\rho_0[\tilde{w}]) = 0. \tag{B7}$$

The associated "residual" mean streamfunction $\widetilde{\Psi}_M$ is derived from the $[\tilde{v}]$ and $[\tilde{w}]$, given by

$$\widetilde{\Psi}_M = \frac{2\pi a\cos\phi}{g}\int_0^p [\tilde{v}]dp. \tag{B8}$$

In this study, the strength of the BDC is estimated from the residual mass stream function.

b. Calculation of the e-folding time scale

The e-folding time scale ($exp(-t/\tau)$) is found by 1) calculating the autocorrelation function; and 2) estimating the linear least squares fit of $exp(-t/\tau)$ to the autocorrelation function at lags of up to 60 days.

c. Calculation of cooling rates and relaxation time scale

The time evolution of the atmospheric temperature can be decomposed into contributions from radiative terms and dynamic terms:

$$\left(\frac{dT}{dt}\right)_{tot} = \left(\frac{dT}{dt}\right)_{rad} + \left(\frac{dT}{dt}\right)_{dyn} \tag{B9}$$

Consider the atmosphere initially at equilibrium, thus

$$\left(\frac{dT}{dt}\right)_{tot,old} = 0. \tag{B10}$$

Then,

$$\left(\frac{dT}{dt}\right)_{rad,old} + \left(\frac{dT}{dt}\right)_{dyn} = 0 \tag{B11}$$

Suppose a small external perturbation (ΔT) on the equilibrium temperature, radiative cooling rates is changed accordingly. So the new temperature (T) relaxes at a new rate:

$$\begin{aligned}\left(\frac{dT}{dt}\right)_{tot,new} = \frac{d\Delta T}{dt} &= \left(\frac{dT}{dt}\right)_{rad,new} + \left(\frac{dT}{dt}\right)_{dyn} \\ &= \left(\frac{dT}{dt}\right)_{rad,new} - \left(\frac{dT}{dt}\right)_{rad,old} \qquad \text{(B12)} \\ &= \frac{\partial}{\partial T}\left(\frac{dT}{dt}\right)_{rad} \Delta T \qquad \text{(B13)}\end{aligned}$$

The radiatively induced time rate of change of temperature due to absorption or emission of radiation within an atmosphere layer is given by:

$$\left(\frac{dT}{dt}\right)_{rad} = \frac{g}{C_p}\frac{dF_{net}}{dp}, \tag{B14}$$

Considering an atmospheric layer, whose radiative cooling rate is dominated by the cooling-to-space mechanism (e.g., Goody and Yung 1989),

$$\begin{aligned}\left(\frac{dT}{dt}\right)_{rad} &= \frac{g}{C_p P_a}(-F^{\uparrow}) \\ &= -\frac{\varepsilon\sigma T^4}{g^{-1}C_p P_a}\end{aligned} \tag{B15}$$

where C_p is the specific heat of air, P_a is the pressure difference between the upper and lower boundaries of the layer, and g is the gravitational acceleration, $F^{\uparrow}$ is the outgoing radiation radiated by this layer, σ is the Stefan- Boltzmann constant, and ε is the effective emissivity of the layer.

Taking the temperature derivative of Eq. (B15)

$$\frac{\partial}{\partial T}\left(\frac{dT}{dt}\right)_{rad} = -\frac{4\varepsilon\sigma T^3}{g^{-1}C_p P_a} \tag{B16}$$

Plug Eq. (B16) into Eq. (B13)

$$\frac{d\Delta T}{dt} = -\frac{4\varepsilon\sigma T^3 \Delta T}{g^{-1}C_p P_a} \tag{B17}$$

So the damping time scale of the temperature anomaly inferred from Eq. (B17) is:

$$\tau = \left(\frac{4\varepsilon\sigma T^3}{g^{-1}C_p P_a}\right)^{-1} \tag{B18}$$

Plug Eq. (B15) into Eq. (B18):

$$\tau = \frac{T}{4}\left(\frac{dT}{dt}\right)^{-1}_{rad} \tag{B19}$$

In general, the larger the local radiative cooling rate the shorter the local radiative relaxation time scale (see for example Wallace and Hobbs 2006, Chapter 4). Similar results are also obtained by estimating the radiative relaxation time scale as the temperature anomaly divided by heating

rate anomaly (e.g., see Eq. 7 in Jucker et al. 2013). Note that the above estimation of the radiative relaxation time scale is accurate to the extent that the total radiative cooling can be approximated by the cooling-to-space term. While this is a generally good approximation in the stratosphere (e.g., Goody and Yung 1989), it neglects the additional radiative cooling (relaxation) due to the radiative fluxes between layers, and the change of radiative fluxes with the Earth's surface. Thus, the estimation offers an upper-bound estimate of the actual relaxation time.

References

Allan, R. P., 2011: Combining satellite data and models to estimate cloud radiative effect at the surface and in the atmosphere. *Meteor. Appl.*, **18**, 324–333.

Andrews, D. G., J. R. Holton, and C. B. Leovy, 1987: *Middle Atmosphere Dynamics*. Academic Press, 489 pp.

Baldwin, M. P., and T. J. Dunkerton, 1999: Propagation of the Arctic Oscillation from the stratosphere to the troposphere. *J. Geophys. Res.*, **104**, 30 937–30 946.

Baldwin, M. P., and T. J. Dunkerton, 2001: Stratospheric harbingers of anomalous weather regimes. *Science*, **294**, 581–584.

Baldwin, M. P., D. B. Stephenson, D. W. J. Thompson, T. J. Dunkerton, A. J. Charlton, and A. O'Neill, 2003: Stratospheric memory and skill of extended range weather forecasts. *Science*, **301**, 636–640.

Birner, T., 2006: Fine-scale structure of the extratropical tropopause region. *J. Geophys. Res.*, **111**, D04 104, doi:10.1029/2005JD006301.

Birner, T., and H. Boñisch, 2011: Residual circulation trajectories and transit times into the extratropical lowermost stratosphere. *Atmos. Chem. Phys.*, **11**, 817–827.

Birner, T., A. Dörnbrack, and U. Schumann, 2002: How sharp is the tropopause at midlatitudes? *Geophys. Res. Lett.*, **29**, 1700, doi:10.1029/2002GL015142.

Bretherton, C. S., P. N. Blossey, and M. Khairoutdinov, 2005: An energy-balance analysis of deep convective self-aggregation above uniform SST. *J. Atmos. Sci.*, **62**, 4273–4292.

Ceppi, P., and D. L. Hartmann, 2016: Clouds and the atmospheric circulation Response to warming. *J. Climate*, **29**, 783–799, doi:10.1002/2014GL060043.

Charney, J. G., and P. G. Drazin, 1961: Propagation of planetary-scale disturbances from the lower into the upper atmosphere. *J. Geophys. Res.*, **66**, 83–109.

Collins, W., and Coauthors, 2008: Evaluation of HadGEM2 model. Technical Note 74, Meteorological Office Hadley Centrr, Princeton, NJ, 47 pp.

Coppin, D., and S. Bony, 2015: Physical mechanisms controlling the initiation of convective self-aggregation in a general circulation model. *J. Adv. Model. Earth Syst*, **7**, 20602078.

Crueger, T., and B. Stevens, 2015: The effect of atmospheric radiative heating by clouds on the Madden-Julian Oscillation. *J. Adv. Model. Earth Syst*, doi:10.1002/2015MS000434.

Davis, S. M., C. K. Liang, and K. H. Rosenlof, 2013: Interannual variability of tropical tropopause layer clouds. *Geophys. Res. Lett.*, **40**, 2862–2866, doi:10.1002/grl.50512.

Dufresne, J.-L., and Coauthors, 2013: Climate change projections using the IPSL-CM5 earth system model: From CMIP3 to CMIP5. *Climate Dyn.*, **40**, 2123–2165, doi:10.1007/s00382-012-1636-1.

Edmon, H. J., B. J. Hoskins, and M. E. McIntyre, 1980: Eliassen-Palm cross sections for the troposphere. *J. Atmos. Sci.*, **37**, 2600–2616.

Eichelberger, S. J., and D. L. Hartmann, 2005: Changes in the strength of the Brewer-Dobson circulation in a simple AGCM. *Geophys. Res. Lett.*, **32**, L15 807, doi:10.1029/2005GL022924.

Fermepin, S., and S. Bony, 2014: Influence of low-cloud radiative effects on tropical circulation and precipitation. *J. Adv. Model. Earth Syst*, **06**, doi:10.1002/2013MS000288.

Forster, P. M., G. Bodeker, R. Schofield, S. Solomon, and D. W. J. Thompson, 2007: Effects of ozone cooling in the tropical lower stratosphere and upper troposphere. *Geophys. Res. Lett.*, **34**, L23 813, doi:10.1029/2007GL031994.

Gerber, E. P., S. Voronin, and L. M. Polvani, 2008: Testing the annular mode autocorrelation time scale in simple atmospheric General Circulation Models. *Mon. Wea. Rev.*, **136**, 1523–1536.

Goody, R. M., and Y. L. Yung, 1989: *Atmospheric Radiation: Theoretical Basis*. Oxford University Press, New York, NY, 544 pp.

Gordon, C., 1992: Comparison of 30-day integrations with and without cloud-radiation interaction. *Mon. Wea. Rev.*, **120**, 1244–1277.

Grise, K. M., and D. W. J. Thompson, 2013: On the signatures of equatorial and extratropical wave forcing in tropical tropopause layer temperatures. *J. Atmos. Sci.*, **69**, 857–874.

Grise, K. M., D. W. J. Thompson, and T. Birner, 2009: On the role of radiative processes in stratosphere-troposphere coupling. *J. Climate*, **22**, 4154–4161, doi:10.1175/2009JCLI2756.1.

476 Hall, A., and S. Manabe, 1999: The role of water vapor feedback unperturbed climate variabil-
477 ity and global warming. *J. Climate*, **45**, 2327–2346, doi:10.1175/1520-0442(1999)012,2327:
478 TROWVF.2.0.CO;2.

479 Harrop, B. E., and D. L. Hartmann, 2016: The role of cloud radiative heating in determining
480 the location of the ITCZ in aquaplanet simulations. *J. Climate*, **29**, 2741–2763, doi:10.1175/
481 JCLI-D-15-0521.1.

482 Haynes, J. M., T. H. V. Haar, T. L'Ecuyer, and D. Henderson, 2013: Radiative heating character-
483 istics of Earths cloudy atmosphere from vertically resolved active sensors. *Geophys. Res. Lett.*,
484 **40**, 624–630, doi:10.1002/grl.50145.

485 Haynes, P. H., M. E. McIntyre, T. G. Shepherd, C. J. Marks, and K. P. Shine, 1991: On the
486 "downward control" of extratropical diabatic circulations by eddy-induced mean zonal forces.
487 *J. Atmos. Sci.*, **48**, 651–680.

488 Hourdin, F., and Coauthors, 2013a: Impact of the LMDZ atmospheric grid configuration on the
489 climate and sensitivity of the IPSL-CM5A coupled model. *Climate Dyn.*, **40**, 2167–2192.

490 Hourdin, F., and Coauthors, 2013b: LMDZ5B: The atmospheric component of the IPSL climate
491 model with revisited parameterizations for clouds and convection. *Climate Dyn.*, **40**, 2193–
492 2222.

493 Jucker, M., S. Fueglistaler, and G. Vallis, 2013: Maintenance of the stratospheric structure in an
494 idealized general circulation model. *J. Atmos. Sci.*, **70**, 3341–3358.

495 Kodera, K., F. B. M., C. Claud, and N. Eguchi, 2015: The role of convective overshooting clouds
496 in tropical stratospheretroposphere dynamical coupling. *Atmos. Chem. Phys.*, **15**, 6767–6774,
497 doi:10.5194/acp-15-6767-2015.

Kodera, K., K. Yamazaki, M. Chiba, and K. Shibata, 1990: Downward propagation of the upper stratospheric mean zonal wind perturbation to the troposphere. *Geophys. Res. Lett.*, **17**, 1263–1266.

Kohma, M., and K. Sato, 2014: Variability of upper tropospheric clouds in thepolar region during stratosphericsudden warmings. *J. Geophys. Res.*, **119**, 10 100–10 113, doi:10.1002/2014JD021746.

Li, Y., and D. W. J. Thompson, 2013: The signature of the stratospheric Brewer-Dobson circulation in tropospheric clouds. *J. Geophys. Res.*, **118**, 3486–3494, doi:10.1002/jgrd.50339.

Li, Y., D. W. J. Thompson, and S. Bony, 2015: The influence of atmospheric cloud radiative effects on the large-scale atmospheric circulation. *J. Climate*, **28**, 7263–7278.

Limpasuvan, V., D. L. Hartmann, D. W. J. Thompson, K. Jeev, and Y. L. Yung, 2005: Stratosphere-troposphere evolution during polar vortex intensification. *J. Geophys. Res.*, **110**, doi:10.1029/2005JD006302.

Limpasuvan, V., D. Thompson, and D. Hartmann, 2004: On the life cycle of Northern Hemisphere stratosphere sudden warming. *J. Geophys. Res.*, **13**, 2584–2596.

Matsuno, T., 1970: Vertical propagation of stationary planetary waves in the winter Northern Hemisphere. *J. Atmos. Sci.*, **27**, 871–883.

Mauritsen, T., R. G. Graversen, D. Klocke, P. L. Langen, B. Stevens, and L. Tomassini, 2013: Climate feedback efficiency and synergy. *Climate Dyn.*, **41**, 2539–2554, doi:10.1007/s00382-013-1808-7.

Merlis, 2015: Direct weakening of tropical circulations from masked CO2 radiative forcing. *Proc. Natl. Acad. Sci.*, **112**, 13 167–13 171, doi:10.1073/pnas.1508268112.

Muller, C. J., and I. M. Held, 2012: Detailed investigation of the self-aggregation of convection in cloud-resolving simulations. *J. Atmos. Sci.*, **69**, 2551–2565.

Muller, C. J., and I. M. Held, 2015: What favors convective aggregation and why? *Geophys. Res. Lett.*, **42**, 5626–5634, doi:10.1002/2015GL064260.

Rädel, G., T. Mauritsen, B. Stevens, D. Dommenget, D. Dommenget, D. Matei, K. Bellomo, and A. Clement, 2016: Amplification of El Niño by cloud longwave coupling to atmospheric circulation. Nature Geoscience. *Nat. Geosci.*, **9**, 106–110.

Randall, D. A., Harshvardhan, D. A., Dazlich, and T. G. Corsett, 1989: Interactions among radiation, convection, and large-scale dynamics in a general circulation model. *J. Atmos. Sci.*, **46**, 1943–1970.

Randel, W. J., R. R. Garcia, and F. Wu, 2008: Dynamical balances and tropical stratospheric upwelling. *J. Atmos. Sci.*, **65**, 3584–3595.

Randel, W. J., M. Park, F. Wu, and N. Livesey, 2007: A large annual cycle in ozone above the tropical tropopause linked to the Brewer-Dobson circulation. *J. Atmos. Sci.*, **64**, 4479–4488.

Schneider, E. K., B. P. Kirtman, and R. S. Lindzen, 1999: Tropospheric water vapor and climate sensitivity. *J. Atmos. Sci.*, **56**, 1649–1658.

Sherwood, S. C., V. Ramanathan, T. P. Barnett, M. K. Tyree, and E. Roeckner, 1994: Response of an atmospheric general circulation model to radiative forcing of tropical clouds. *J. Geophys. Res.*, **99**, 20 829–20 845.

Simmons, A., S. Uppala, D. Dee, and S. Kobayashi, 2007: ERA-Interim: New ECMWF reanalysis products from 1989 onwards. *ECMWF Newsletter*, **110**, 25–35, ECMWF, Reading, United Kingdom.

Slingo, A., and J. M. Slingo, 1988: The response of a general circulation model to cloud longwave radiative forcing. I: Introduction and initial experiments. *Quart. J. Roy. Meteor. Soc.*, **114**, 1027–1062.

Slingo, J. M., and A. Slingo, 1991: The response of a general circulation model to cloud longwave radiative forcing. II: Further studies. *Quart. J. Roy. Meteor. Soc.*, **117**, 333–364.

Sterl, A., and Coauthors, 2012: A look at the ocean in the EC-Earth climate model. *Climate Dyn.*, **39**, 2631–2657.

Stevens, B., S. Bony, and M. Webb, 2012: Clouds on-off klimate intercomparison experiment (COOKIE). Tech. rep. [Available online at http://www.euclipse.eu/downloads/Cookie.pdf.].

Stevens, B., and Coauthors, 2013: Atmospheric component of the MPI-M earth system model: ECHAM6. Journal of Advances in Modeling Earth System. *J. Adv. Model. Earth Syst*, **5**, 146–172.

Taguchi, M., and D. L. Hartmann, 2006: Increased occurrence of stratospheric sudden warmings during El Niño as simulated by WACCM. *J. Climate*, **19**, 324–332.

Tian, B., and V. Ramanathan, 2003: A simple moist tropical atmosphere model: The role of cloud radiative forcing. *J. Climate*, **16**, 2086–2092.

Ueyama, R., E. P. Gerber, J. M. Wallace, and D. M. W. Frierson, 2013: The role of high-latitude waves in the intraseasonal to seasonal variability of tropical upwelling in the Brewer-Dobson circulation. *J. Atmos. Sci.*, **70**, 1631–1648.

Ueyama, R., and J. M. Wallace, 2010: To what extent does highlatitude wave forcing drive tropical upwelling in the Brewer-Dobson circulation? *J. Atmos. Sci.*, **67**, 1232–1246.

563 Vallis, G. K., 2006: *Atmospheric and Oceanic Fluid Dynamics: Fundamentals and Large-Scale*
564 *Circulation*. Cambridge University Press, Cambridge, U.K., 561 pp.

565 Voigt, A., S. Bony, J.-L. Dufresne, and B. Stevens, 2014: The radiative impact of clouds on the
566 shift of the inter-tropical convergence zone. *Geophys. Res. Lett.*, **41**, 4308–4315, doi:10.1002/
567 2014GL060354.

568 Voigt, A., and T. A. Shaw, 2015: Radiative changes of clouds and water vapor shape circulation
569 response to global warming. *Nat. Geosci.*, **8**, 102106, doi:10.1038/ngeo2345.

570 Voigt, A., and T. A. Shaw, 2016: Impact of regional longwave cloud-radiative changes on the
571 extratropical jet stream response to global warming. *J. Climate*, revised.

572 Voldoire, A., and Coauthors, 2013: The CNRM-CM5.1 global climate model: Description and
573 basic evaluation. *Climate Dyn.*, **40**, 2091–212.

574 Wallace, J. M., and P. V. Hobbs, 2006: *Atmospheric Science: An Introductory Survey*. 2nd ed.,
575 Academic Press, 483 pp.

576 Webb, M. J., and Coauthors, 2016: The Cloud Feedback Model Intercomparison Project (CFMIP)
577 contribution to CMIP6. *Geosci. Model Dev. Discuss*, doi:10.5194/gmd-2016-70.

578 Wetherald, R. T., and S. Manabe, 1980: Cloud cover and climate sensitivity. *J. Atmos. Sci.*, **37**,
579 1485–1510, doi:10.1175/1520-0469(1980)037,1485:CCACS.2.0.CO;2.

580 Wetherald, R. T., and S. Manabe, 1988: Cloud feedback processes in a general circulation model.
581 *J. Atmos. Sci.*, **45**, 1397–1416, doi:10.1175/1520-0469(1988)045,1397:CFPIAG.2.0.CO;2.

582 Wing, A. A., and K. A. Emanuel, 2014: Physical mechanisms controlling self-aggregation of
583 convection in idealized numerical modeling simulations. *J. Adv. Model. Earth Syst*, **6**, 59–74.

584 Yukimoto, S., and Coauthors, 2012: A New Global Climate Model of the Meteorological Research
585 805 Institute: MRI-CGCM3: Model Description and Basic Performance. *J. Meteor. Soc. Japan*,
586 **90A**, 23–64.

587 Yulaeva, E., J. Holton, and J. M. Wallace, 1994: On the cause of the annual cycle in tropical
588 lower-stratospheric temperatures. *J. Atmos. Sci.*, **51**, 169–174.

LIST OF TABLES

Table 1. Model descriptions and details. 32

Table 2. Summary statistics for the fields indicated based on seven available COOKIE models. The results are not sensitive to details of the analysis: similar results were found for averages over slightly different latitude band and vertical level. The statistical significance of the results is estimated using the Student's *t* statistic for the difference in means between clouds-on and clouds-off experiments. Since the results for the IPSL-CM5A-LR provide an a priori expectation of the sign of the results, confidence levels are based on a one-tailed test of the difference in sample means. Bolded values indicate where differences are significant at the 99% confidence level based on a one-tailed test of the *t* statistic. 33

TABLE 1. Model descriptions and details.

Modeling Center	Model Name	Atmospheric Resolution lon × lat, level	Citations
Instiut Pierre-Simon Laplace (IPSL; France)	IPSL-CM5A-LR (IPSL Coupled Model, version 5A, low resolution)	3.75° × 1.875°, L39	Dufresne et al. (2013) Hourdin et al. (2013a)
Instiut Pierre-Simon Laplace (IPSL; France)	IPSL-CM5B-LR (IPSL Coupled Model, version 5B, low resolution)	3.75° × 1.875°, L31	Dufresne et al. (2013) Hourdin et al. (2013b)
Centre National de Recherches Meteorologiques (CNRM; France)	CNRM-CM5 (CNRM Coupled Global Climate Model, version 5	1.41° × 1.40°, L39	Voldoire et al. (2013)
Met Office Hadley Centre (MOHC; U.K.)	HadGEM2-A (Hadley Global Environment Model 2-Atmosphere)	1.25° × 1.875°, L38	Collins et al. (2008)
Max Planck Institute for Meteorology (MPI-M; Germany)	ECHAM-6 (Atmospheric component of the MPI-M Earth System Model)	1.875° × 1.8653°, L31	Stevens et al. (2013)
Meteorological Research Institute (MRI; Japan)	MRI-CGCM3 (MRI Coupled General Circulation Model, version 3)	1.125° × 1.12°, L48	Yukimoto et al. (2012)
Jointly developed by several European institutes and ECMWF	EC-EARTH	1.125° × 1.12°, L62	Sterl et al. (2012)

TABLE 2. Summary statistics for the fields indicated based on seven available COOKIE models. The results are not sensitive to details of the analysis: similar results were found for averages over slightly different latitude band and vertical level. The statistical significance of the results is estimated using the Student's t statistic for the difference in means between clouds-on and clouds-off experiments. Since the results for the IPSL-CM5A-LR provide an a priori expectation of the sign of the results, confidence levels are based on a one-tailed test of the difference in sample means. Bolded values indicate where differences are significant at the 99% confidence level based on a one-tailed test of the t statistic.

	warming in the upper polar stratosphere and cooling in the lower tropical stratosphere (implying the strengthening of the BDC)		weakening of the polar vortex (implying increased wave fluxes in extratropical stratosphere)	weakening of N^2 near the tropical tropopause transition layer (TTL)	cooling in the extratropical lower stratosphere	strengthening of N^2 near the extratropical tropopause inversion layer (TIL)
Model	$[\mathrm{T}]_{10mb}^{50^\circ-70^\circ S/N}$	$[\mathrm{T}]_{70mb}^{30^\circ S-30^\circ N}$	$[\mathrm{U}]_{50mb}^{50^\circ-70^\circ S/N}$	$[N^2]_{100mb}^{30^\circ S-30^\circ N}$	$[\mathrm{T}]_{200mb}^{40^\circ-70^\circ S/N}$	$[N^2]_{150mb}^{50^\circ-70^\circ S/N}$
IPSL-CM5A-LR	**4.28** / **2.39**	**−4.84**	**−3.71** / **−3.16**	**−0.51**	**−6.03** / **−6.00**	**0.39** / **0.53**
IPSL-CM5B-LR	**4.40** / **1.19**	**−5.95**	**−8.50** / **−4.51**	**−0.39**	**−3.74** / **−5.00**	**0.29** / **0.49**
CNRM-CM5	**0.96** / 0.08	**−4.75**	**−3.90** / −0.10	**−0.42**	−0.16 / **−1.30**	**0.02** / **0.05**
HadGEM2-A	**0.99** / **0.92**	**−1.47**	**−1.31** / **−1.59**	**−0.18**	**−1.07** / **−1.38**	**0.13** / **0.21**
MPI-ECHAM6	**2.68** / **1.45**	**−3.52**	**−2.75**/**−1.48**	**−0.39**	**−0.30**/**−1.23**	**0.14** / **0.25**
MRI-CGCM3	**1.35** / **1.19**	**−2.47**	0.33 / −0.80	**−0.51**	**−0.21** / 0.31	**0.03** / **0.07**
EC-Earth	**1.15** / **1.05**	1.12	**−1.07** / 0.64	**−0.18**	**−1.09** / 0.21	0.01 / 0.00

LIST OF FIGURES

Fig. 1. Comparing the long-term mean, zonal-mean circulation of the (left) clouds-on experiment and (right) ERA-interim reanalysis for the fields indicated. The EP flux divergence (D_F; see Eq. B3) is contoured at -1, 1, 3 m s^{-1} day^{-1} etc (solid contours are divergence and dashed contours are convergence). The thick black line indicates the long-term mean tropopause height. Tropopause height is identified using the World Meteorological Organization lapse rate definition. The long-term mean denotes the mean over all 30 years (1979–2008) of the integration in the clouds-on experiment, and over the period 1979–2008 for ERA-Interim. . . . 36

Fig. 2. The long-term-mean, zonal-mean longwave component of the atmospheric cloud radiative effects in the clouds-on experiment. The thick solid line superimposed on each panel indicates the long-term mean tropopause height in the clouds-on experiment. The results are reproduced from Li et al. (2015), but the pressure coordinate is plotted on a logarithmic scale consistent with the following figures. 37

Fig. 3. Differences in the long-term mean, zonal-mean atmospheric circulation between the clouds-on and clouds-off experiments for a) zonal-mean temperature, b) zonal-mean zonal wind, c) residual mass streamfunction. The dashed lines in all panels indicate the long-term mean tropopause height in the clouds-off experiment. Stippling indicates differences that are significant at the 99% level based on a two-tailed test of the t statistic. The solid line in (a) indicates the long-term mean tropopause height in the clouds-on experiment. The responses in residual mass streamfunction below the tropopause are noisy and difficult to interpret, and are masked out. 38

Fig. 4. Differences in the long-term mean, zonal-mean atmospheric circulation between the clouds-on and clouds-off experiments for a) the EP flux, b) the wavenumber decomposition of the vertical component EP flux averaged between 200–500 hPa and c) the wavenumber decomposition of the meridional EP flux averaged between 200–300 hPa. Stippling indicates differences that are significant at the 99% level based on a two-tailed test of the t statistic. . . 39

Fig. 5. Differences in the long-term mean, zonal-mean circulation between the clouds-on and clouds-off experiments for a) static stability and b) cloud fraction. The static stability (N^2) is defined as $\frac{g}{\theta}\frac{\partial\theta}{\partial z}$, where g is 9.81 m s^{-2} and θ is potential temperature. Stippling indicates differences that are significant at the 99% level based on a two-tailed test of the t statistic. The dashed lines in all panels indicate the long-term mean tropopause height in the clouds-off experiment. 40

Fig. 6. Seasonal cycle of differences between the clouds-on and clouds-off experiments in the long-term mean, zonal-mean a) cloud longwave radiative heating rates averaged between 200–300 hPa, b) wavenumbers 4–6 component of vertical EP flux averaged between 200–300 hPa, and c) cloud fraction averaged between 200–300 hPa. Note for panel a, the cloud radiative heating rates are uniformly zero in clouds-off simulations by experimental design. Stippling in panel b and c indicates differences that are significant at the 99% level based on a two-tailed test of the t statistic. 41

Fig. 7. Latitude-height cross section of the e-folding time scale of the autocorrelation function of the zonal-mean (top) zonal wind and (bottom) temperature anomalies for the NH winter season months January–March (JFM). Results based on the clouds-on experiments are shown on the left panel, and clouds-off experiments on the right panel. The thick solid (dashed) black line indicates the long-term mean tropopause height in clouds-on (clouds-off) experiments. . . 42

Fig. 8. Regressions of zonal-mean zonal wind anomalies averaged between 55°–75°N onto standardized values of the zonal-mean zonal wind anomalies at 10 hPa during JFM season as a function of pressure level and lag. Results based on the clouds-on experiments are shown on the left panel, and clouds-off experiments on the right panel. 43

Fig. 9. Schematic diagram summarizing the basic impacts of cloud radiative effects on the zonal-mean stratospheric circulation, as revealed in this study. The background shading is reproduced from Fig. 2 and indicates the longwave component of atmospheric cloud radiative effects in the clouds-on experiment; the solid black line indicates the long-term mean tropopause height from the clouds-on experiment. The broad grey arrows illustrate the changes in the wave activity flux, and thin blue arrows denote the changes in the longwave radiative flux. The red and blue stippling indicates regions of warm and cold temperature anomalies, respectively. The thick black arrows illustrate the changes in the Brewer-Dobson Circulation. 44

Fig. 10. The long-term-mean, zonal-mean, vertically integrated atmospheric cloud radiative effects in the clouds-on experiment for seven models listed in Table 1. 45

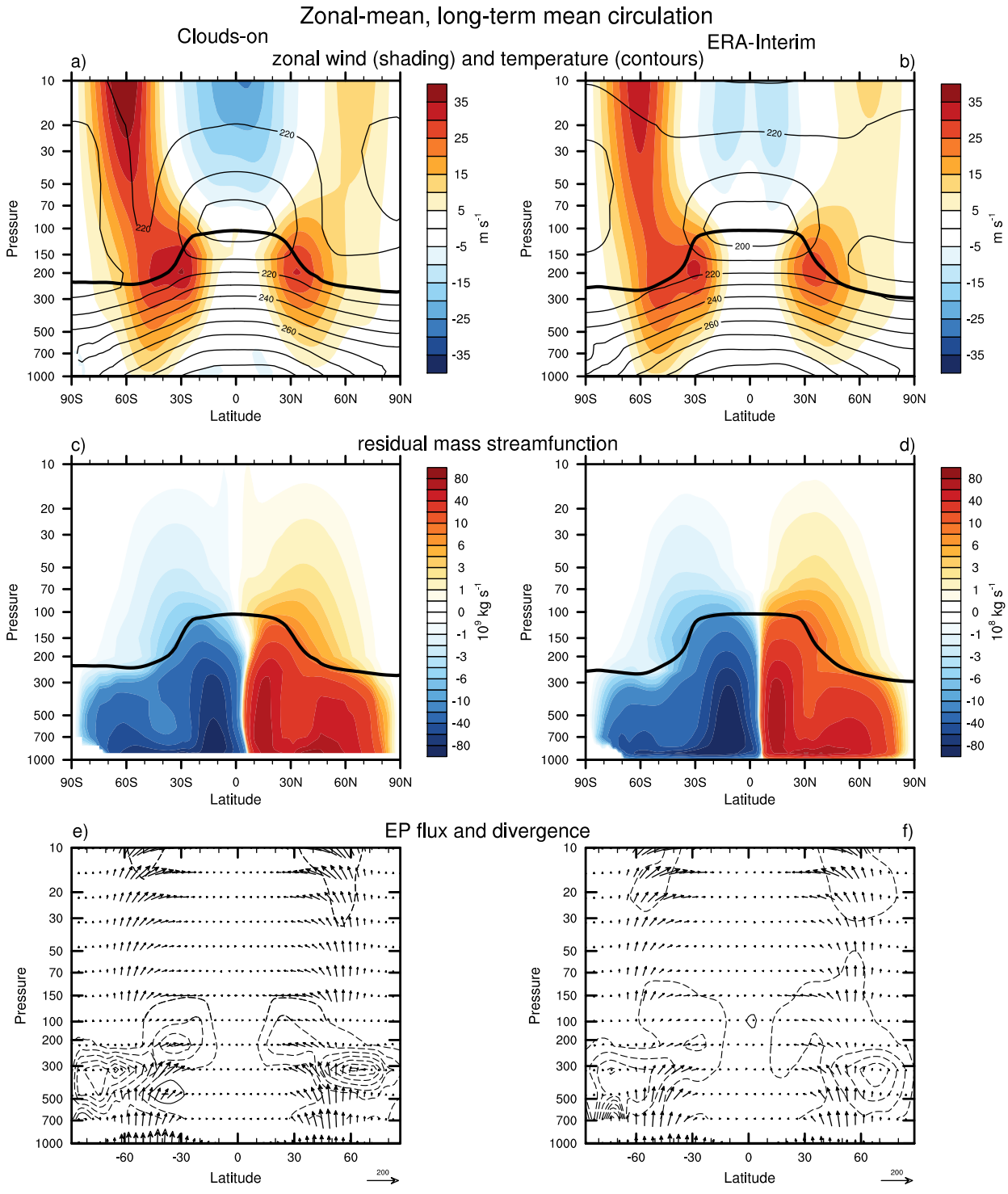

666 FIG. 1. Comparing the long-term mean, zonal-mean circulation of the (left) clouds-on experiment and (right)
667 ERA-interim reanalysis for the fields indicated. The EP flux divergence (D_F; see Eq. B3) is contoured at -1,
668 1, 3 m s^{-1} day^{-1} etc (solid contours are divergence and dashed contours are convergence). The thick black line
669 indicates the long-term mean tropopause height. Tropopause height is identified using the World Meteorological
670 Organization lapse rate definition. The long-term mean denotes the mean over all 30 years (1979–2008) of the
671 integration in the clouds-on experiment, and over the period 1979–2008 for ERA-Interim.

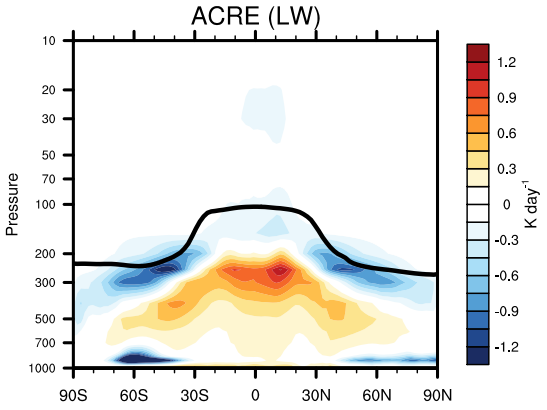

672 FIG. 2. The long-term-mean, zonal-mean longwave component of the atmospheric cloud radiative effects
673 in the clouds-on experiment. The thick solid line superimposed on each panel indicates the long-term mean
674 tropopause height in the clouds-on experiment. The results are reproduced from Li et al. (2015), but the pressure
675 coordinate is plotted on a logarithmic scale consistent with the following figures.

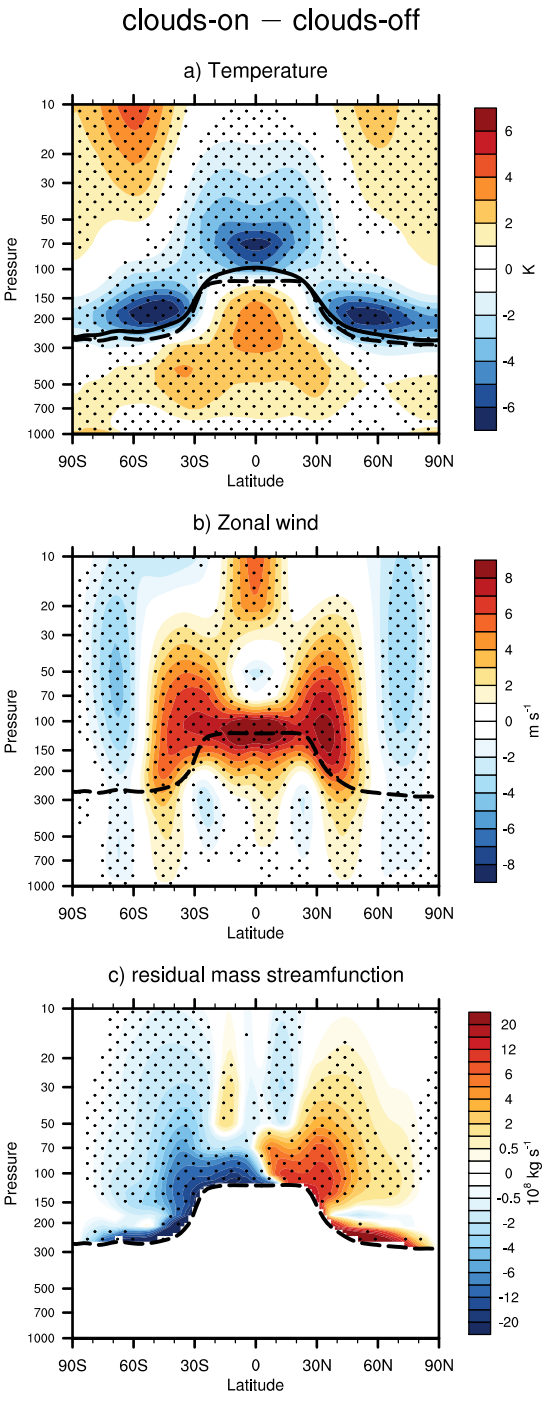

FIG. 3. Differences in the long-term mean, zonal-mean atmospheric circulation between the clouds-on and clouds-off experiments for a) zonal-mean temperature, b) zonal-mean zonal wind, c) residual mass streamfunction. The dashed lines in all panels indicate the long-term mean tropopause height in the clouds-off experiment. Stippling indicates differences that are significant at the 99% level based on a two-tailed test of the t statistic. The solid line in (a) indicates the long-term mean tropopause height in the clouds-on experiment. The responses in residual mass streamfunction below the tropopause are noisy and difficult to interpret, and are masked out.

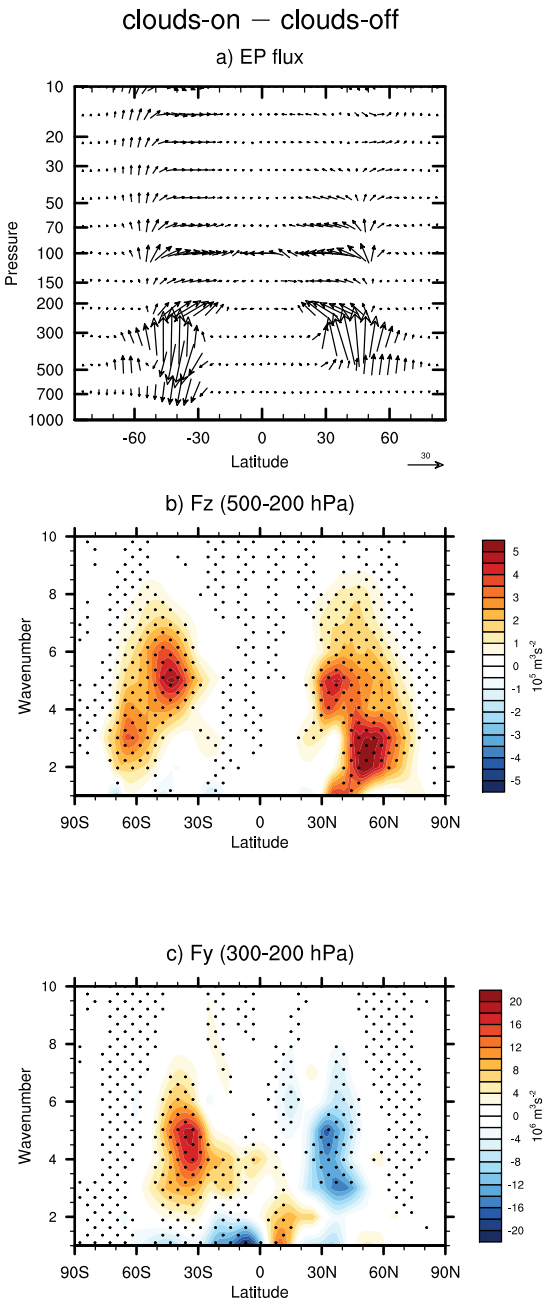

682 FIG. 4. Differences in the long-term mean, zonal-mean atmospheric circulation between the clouds-on and
683 clouds-off experiments for a) the EP flux, b) the wavenumber decomposition of the vertical component EP
684 flux averaged between 200–500 hPa and c) the wavenumber decomposition of the meridional EP flux averaged
685 between 200–300 hPa. Stippling indicates differences that are significant at the 99% level based on a two-tailed
686 test of the *t* statistic.

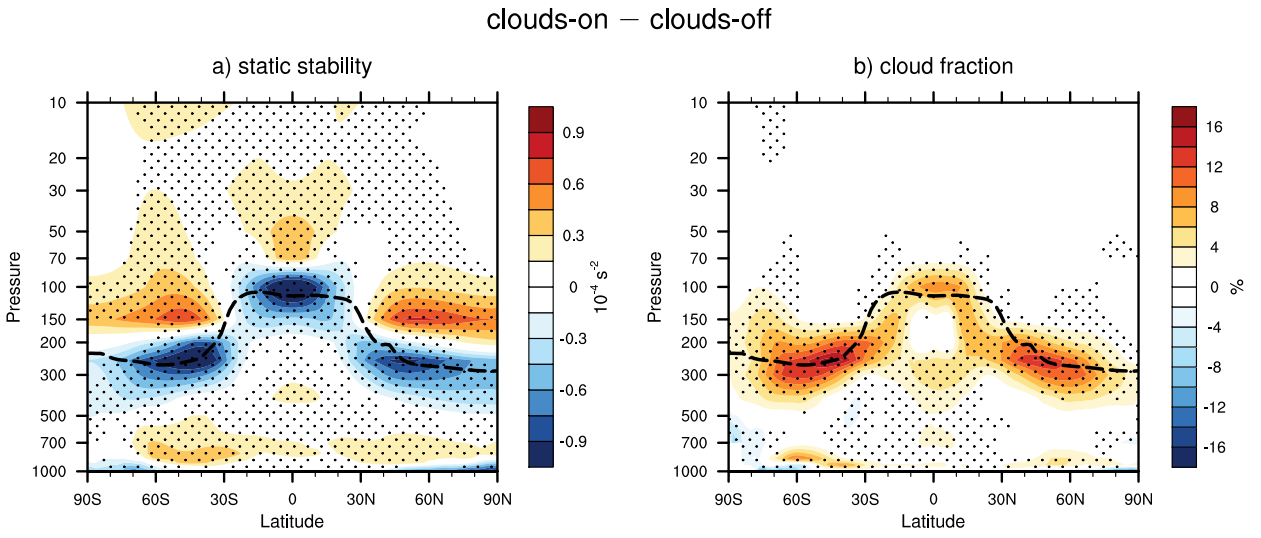

687 FIG. 5. Differences in the long-term mean, zonal-mean circulation between the clouds-on and clouds-off
688 experiments for a) static stability and b) cloud fraction. The static stability (N^2) is defined as $\frac{g}{\theta}\frac{\partial\theta}{\partial z}$, where g is
689 9.81 m s^{-2} and θ is potential temperature. Stippling indicates differences that are significant at the 99% level
690 based on a two-tailed test of the t statistic. The dashed lines in all panels indicate the long-term mean tropopause
691 height in the clouds-off experiment.

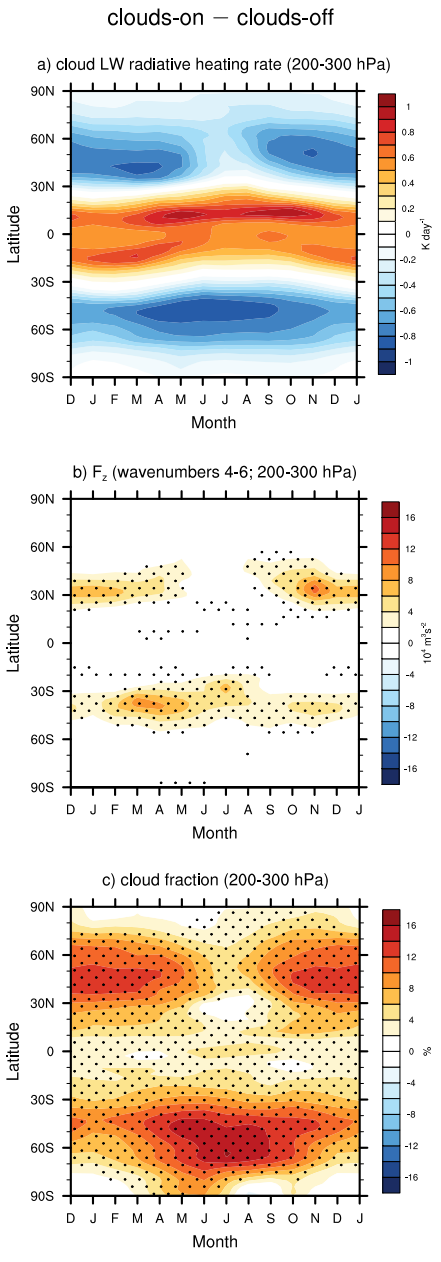

692 FIG. 6. Seasonal cycle of differences between the clouds-on and clouds-off experiments in the long-term
693 mean, zonal-mean a) cloud longwave radiative heating rates averaged between 200–300 hPa, b) wavenumbers
694 4–6 component of vertical EP flux averaged between 200–300 hPa, and c) cloud fraction averaged between
695 200–300 hPa. Note for panel a, the cloud radiative heating rates are uniformly zero in clouds-off simulations by
696 experimental design. Stippling in panel b and c indicates differences that are significant at the 99% level based
697 on a two-tailed test of the *t* statistic.

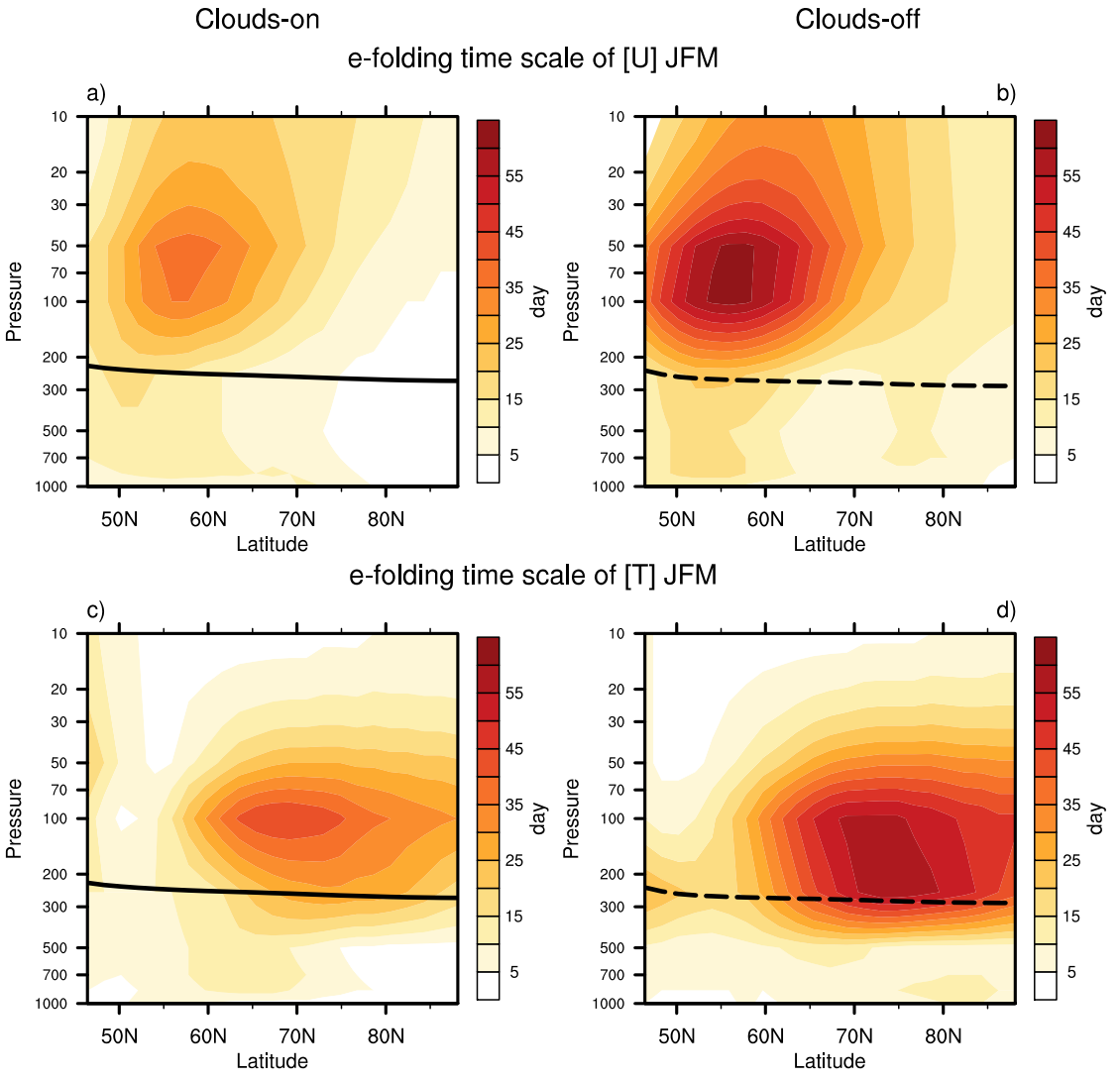

FIG. 7. Latitude-height cross section of the *e*-folding time scale of the autocorrelation function of the zonal-mean (top) zonal wind and (bottom) temperature anomalies for the NH winter season months January–March (JFM). Results based on the clouds-on experiments are shown on the left panel, and clouds-off experiments on the right panel. The thick solid (dashed) black line indicates the long-term mean tropopause height in clouds-on (clouds-off) experiments.

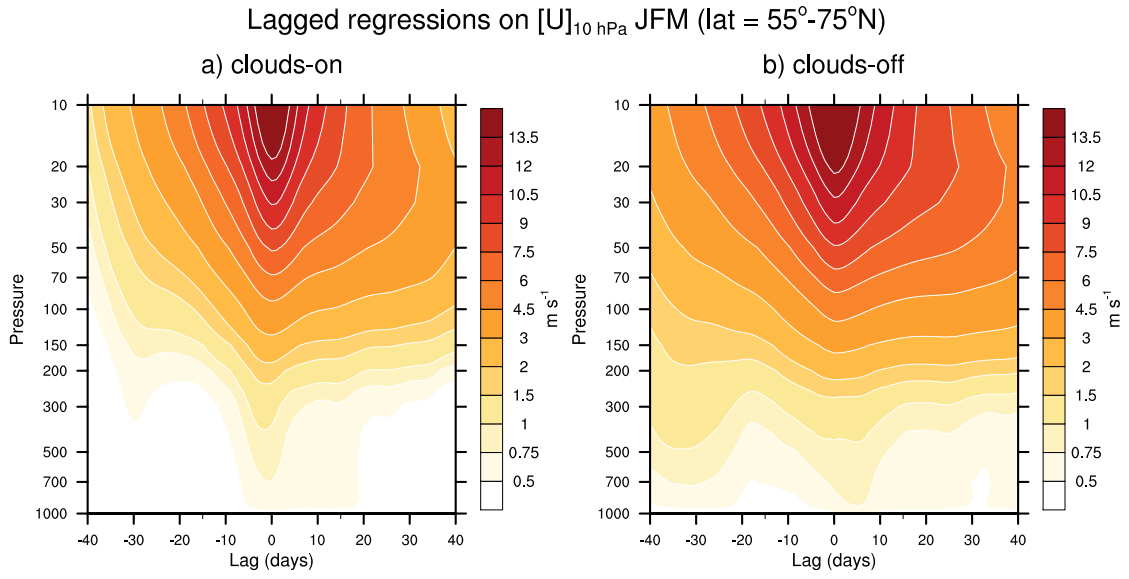

703 FIG. 8. Regressions of zonal-mean zonal wind anomalies averaged between 55°–75°N onto standardized
704 values of the zonal-mean zonal wind anomalies at 10 hPa during JFM season as a function of pressure level and
705 lag. Results based on the clouds-on experiments are shown on the left panel, and clouds-off experiments on the
706 right panel.

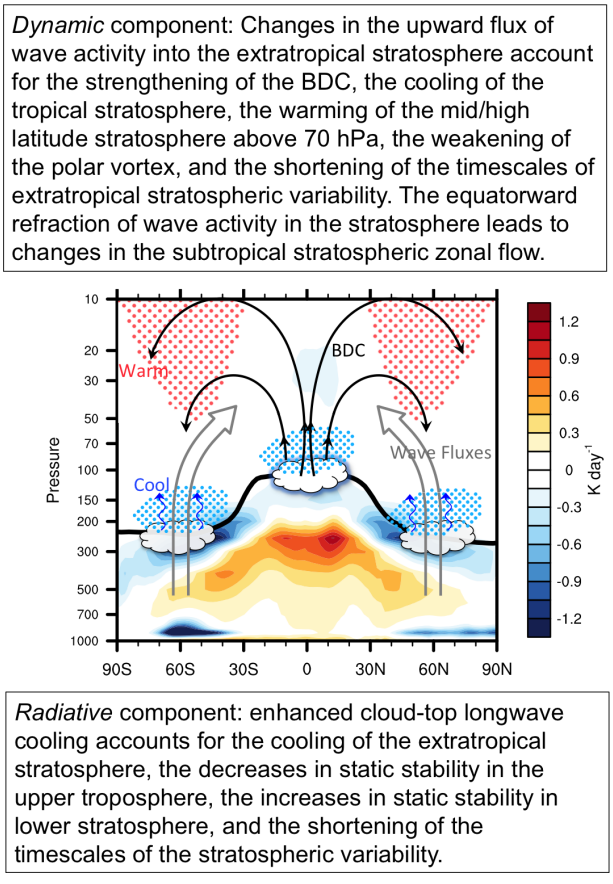

FIG. 9. Schematic diagram summarizing the basic impacts of cloud radiative effects on the zonal-mean stratospheric circulation, as revealed in this study. The background shading is reproduced from Fig. 2 and indicates the longwave component of atmospheric cloud radiative effects in the clouds-on experiment; the solid black line indicates the long-term mean tropopause height from the clouds-on experiment. The broad grey arrows illustrate the changes in the wave activity flux, and thin blue arrows denote the changes in the longwave radiative flux. The red and blue stippling indicates regions of warm and cold temperature anomalies, respectively. The thick black arrows illustrate the changes in the Brewer-Dobson Circulation.

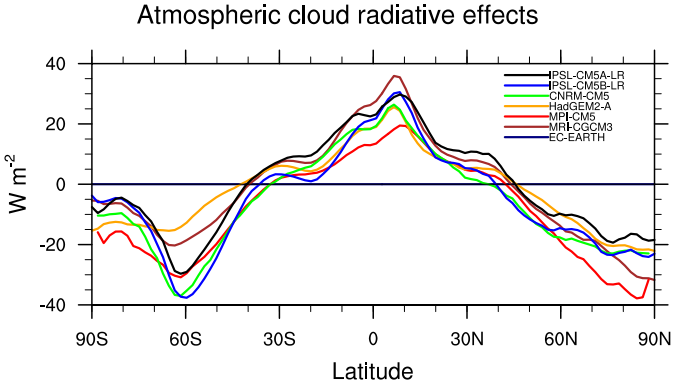

FIG. 10. The long-term-mean, zonal-mean, vertically integrated atmospheric cloud radiative effects in the clouds-on experiment for seven models listed in Table 1.